Geophysical Prospecting

EAGE EUROPEAN ASSOCIATION OF GEOSCIENTISTS & ENGINEERS

Geophysical Prospecting doi: 10.1111/j.1365-2478.2012.01132.x

Measurement of the normal/tangential fracture compliance ratio (Z_N/Z_T) during hydraulic fracture stimulation using S-wave splitting data

James P. Verdon[1]* and Andreas Wüstefeld[2]

[1]*School of Earth Sciences, University of Bristol, UK and* [2]*ESG Ltd, Kingston, Canada*

Received January 2012, revision accepted June 2012

ABSTRACT

We develop a method to invert S-wave splitting (SWS) observations, measured on microseismic event data, for the ratio of normal to tangential compliance (Z_N/Z_T) of sets of aligned fractures. We demonstrate this method by inverting for Z_N/Z_T using SWS measurements made during hydraulic fracture stimulation of the Cotton Valley tight gas reservoir, Texas. When the full SWS data set is inverted, we find that $Z_N/Z_T = 0.74 \pm 0.04$. Windowing the data by time, we were able to observe variations in Z_N/Z_T as the fracture stimulation progresses. Most notably, we observe an increase in Z_N/Z_T contemporaneous with proppant injection. Rock physics models and laboratory observations have shown that Z_N/Z_T can be sensitive to (1) the stiffness of the fluid filling the fracture, (2) the extent to which this fluid can flow in and out of the fracture during the passage of a seismic wave and (3) the internal architecture of the fracture, including the roughness of the fracture surfaces, the number and size of any asperities and the presence of material filling the fracture. These factors have direct implications for modelling the fluid-flow properties of fractures. Consequently, the ability to image Z_N/Z_T using SWS will provide useful information about fractured rocks and allow additional constraints to be placed on reservoir behaviour.

Key words: Microseismic, Fracture, S-wave splitting.

INTRODUCTION

The speed of seismic waves propagating through a fractured rock is modulated by the physical properties of the fracture network. The effect of a fracture network on seismic wavespeeds is determined by its compliance, which in turn is controlled by a variety of physical properties of both the fractures and the background, unfractured rock. The compliance of a fracture set can be further resolved into the compliance of the fractures under normal and under tangential deformation – the normal and tangential compliances, Z_N and Z_T respectively. This paper is focused on measuring the ratio of these compliances, Z_N/Z_T, during hydraulic fracture stimulation and on understanding what Z_N/Z_T can tell us about the physical properties of fractures.

*E-mail: James.Verdon@bris.ac.uk

Attempts to measure Z_N/Z_T in laboratory tests or in the field (see Table 1) have in the main been motivated by the need to calibrate effective medium or discrete fracture network models used to simulate wave propagation through fractured rocks (e.g., Sayers and den Boer 2012, who used values for Z_N/Z_T measured by Lubbe *et al.* 2008). In combination with a menagerie of rock physics models, these experiments indicated that Z_N/Z_T will be influenced by the stiffness of the fluid filling the fracture, as well as terms that describe the internal architecture of the fractures. However, observations pertaining to Z_N/Z_T, with which these models might be calibrated, are sparse.

As well as the need to constrain Z_N/Z_T to model wave propagation through fractured rocks, we consider the lack of measurement of Z_N/Z_T to be a missed opportunity for reservoir characterization. This is because an accurate measurement of Z_N/Z_T might be used to image (1) the stiffness

of fluids saturating the fractures, (2) the connectivity between fractures and pore space and (3) the roughness of fracture faces and/or presence of detrital or diagenetic material filling the fracture. Such observations will be of direct relevance to fluid flow through the fractures and therefore to reservoir productivity. To address this missed opportunity, we developed an approach to invert S-wave splitting (SWS) measurements made on microseismic data for Z_N/Z_T. To do so we extend the inversion approach developed in Verdon and Kendall (2011) and Verdon, Kendall and Wüstefeld (2009), adding Z_N/Z_T as an additional free parameter. In this paper we demonstrate the method by inverting SWS measurements made on microseismic data collected during hydraulic fracture stimulation at Cotton Valley, Texas.

MODELLING AND MEASURING THE EFFECTS OF Z_N/Z_T ON SEISMIC WAVES

The effects of fractures on seismic wave propagation can be modelled using the additional compliance approach developed by Schoenberg and Sayers (1995). The overall compliance of the system of fractured rock ($\mathbf{S}$) is the sum of the compliance of the intact, unfractured rock ($\mathbf{S}^r$) and the additional compliance introduced by the presence of the fractures ($\Delta\mathbf{S}$),

$$\mathbf{S} = \mathbf{S}^r + \Delta\mathbf{S}, \tag{1}$$

where $\mathbf{S}$, $\mathbf{S}^r$ and $\Delta\mathbf{S}$ are 4th order, $3 \times 3 \times 3 \times 3$ tensors. Assuming that the fractures are rotationally symmetrical around the fracture normals, the additional compliance term for a fracture set aligned in the $x_2 - x_3$ plane can be written (in contracted Voigt notation) in terms of the normal and tangential compliances, Z_N and Z_T, of the fracture set,

$$\Delta\mathbf{S} = \begin{pmatrix} Z_N & 0 & 0 & 0 & 0 & 0 \\ 0 & 0 & 0 & 0 & 0 & 0 \\ 0 & 0 & 0 & 0 & 0 & 0 \\ 0 & 0 & 0 & 0 & 0 & 0 \\ 0 & 0 & 0 & 0 & Z_T & 0 \\ 0 & 0 & 0 & 0 & 0 & Z_T \end{pmatrix}. \tag{2}$$

This tensor can be rotated to give the additional compliance of a fracture set with arbitrary orientation. A number of possibilities exist to model Z_N and Z_T. A common approach is to assume that the fractures can be represented by 'penny-shaped' voids (e.g., Hudson 1981; Sayers and Kachanov 1995; Hudson, Liu and Crampin 1996a). For such a case, Z_N/Z_T is controlled by the presence or absence of fluid filling the fractures. If the fractures are drained (Sayers and Kachanov 1995),

$$Z_N/Z_T = 1 - \nu/2, \tag{3}$$

where ν is the Poisson's ratio of the intact rock. For typical reservoir rocks, $\nu \approx 0.25$, implying that for drained, penny-shaped fractures, $Z_N/Z_T \approx 1$. Fracture sets where $Z_N/Z_T = 1$ are considered to be a special case, referred to as 'scalar' fracture sets (Schoenberg and Sayers 1995).

If hydraulically isolated, the presence of a stiff fluid in a fracture serves to reduce Z_N while leaving Z_T unchanged, such that $Z_N/Z_T \to 0$ (e.g., Hudson 1981). However, if fluids can flow between fractures, or between fractures and the rock porosity, then Z_N/Z_T will be governed by the time taken for the fluid to flow out of the fracture (relative to the seismic wave frequency), which is controlled by fracture connectivity and bulk rock permeability, as well as fluid viscosity (e.g., Hudson *et al.* 1996a; Pointer, Liu and Hudson 2000; Chapman 2003). If fluid can escape from the fracture on the timescale of a seismic wave, then Z_N/Z_T will be close to the drained case (equation (3)). If the fluid is too viscous, the permeability of the rock too low, or the frequency of the seismic wave too high, then the fluid will not have time to escape the fracture, it will appear hydraulically isolated and $Z_N/Z_T \to 0$. Chapman (2003) and Hudson *et al.* (1996a) developed rock physics models to account for these frequency-dependent, dispersive effects.

The above models make the assumption that the fractures are penny shaped, meaning that the fracture faces are smooth and do not touch (except at the fracture tips) and there is no detrital or diagenetic infilling material. Microscale imaging of fractures (e.g., Batzle, Simmons and Siegfried 1980) has shown that penny-shaped cracks may well be an overly simplistic representation of real fractures. Barton (2007) argued from a rock mechanics perspective that the fundamental differences between normal and tangential displacements – one involving 'closure', the other involving 'slip' – mean that there is no justification for assuming *a priori* that Z_N/Z_T should be close to 1, regardless of fluid fill. Alternative methods have been developed to compute the compliance via a more detailed description of the internal architecture of the fracture, including terms that describe the contact of asperities or the roughness of the fracture faces. Hudson, Liu and Crampin (1996b) modelled a fracture as a set of isolated elliptical inclusions along a plane, while Hudson, Liu and Crampin (1997) modelled a fracture as a set of isolated welds between two loosely bonded surfaces. In both cases information about the size and number density of voids or welds must be provided (or assumed). Alternatively, Yoshioka and Scholz (1989a,b) measured

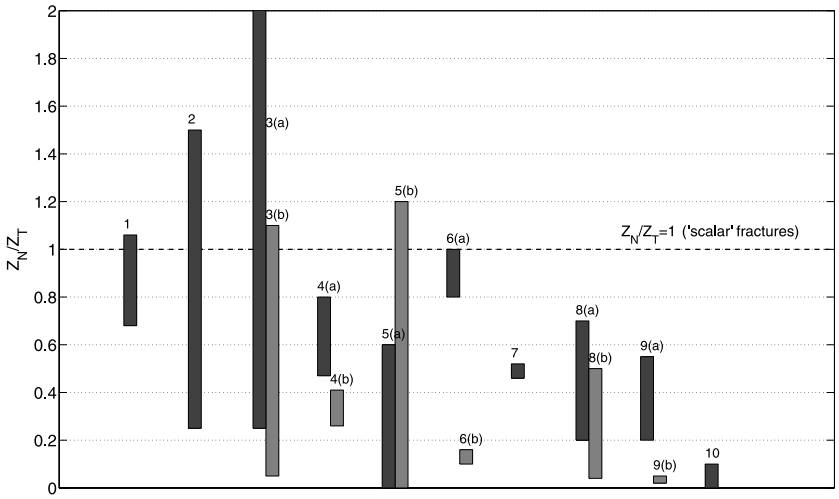

Figure 1 Published values of Z_N/Z_T from laboratory and field studies. Label numbers correspond to the studies listed in Table 1.

fracture surface roughness using a stylus profileometer and thus obtained data to model a fracture as two compressed rough surfaces. Sayers, Taleghani and Adachi (2009) used numerical techniques to simulate the effects on Z_N and Z_T of bridging material in the fracture, such as diagenetic cements or clay and mineral detritus. These studies have made it clear that Z_N/Z_T has the potential to vary significantly depending on the internal architecture and fluid fill of the fracture. Therefore, to learn more about realistic values for Z_N/Z_T, we now consider measurements made in the laboratory and in the field.

Published measurements of the Z_N/Z_T ratio

In Fig. 1 we plot published measurements of Z_N/Z_T made in laboratory and field studies. The studies from which these values were taken are summarized in Table 1. These studies can be divided into a number of subgroups: measurements on core samples that do not contain discrete fractures, intended to image grain-scale discontinuities (Sayers 1999; Sayers and Han 2002; MacBeth and Schuett 2007; Verdon *et al.* 2008; Angus *et al.* 2009); measurements on representative or synthetic samples containing a known crack distribution (Hsu and Schoenberg 1993; Rathore *et al.* 1994); measurements on core samples containing a single, larger-scale fracture (Pyrak-Nolte, Myer and Cook 1990; Lubbe *et al.* 2008); and finally, one field-scale measurement using hammer seismics (Hobday and Worthington 2012).

Verdon *et al.* (2008) and Angus *et al.* (2009) inverted multi-axial ultrasonic measurements made on core samples for Z_N/Z_T. Because these samples do not contain fractures, these measurements were intended to determine the compliance of grain-scale 'micro-fractures'. Using a suite of samples from the Clair oilfield (UK Continental Shelf), Verdon *et al.* (2008) found $0.68 < Z_N/Z_T < 1.06$. Using a wider range of data taken from the literature, Angus *et al.* (2009) found $0.25 < Z_N/Z_T < 1.5$. Similarly, Sayers and Han (2002) inverted ultrasonic measurements made by Han, Nur and Morgan (1986) on both dry and water-saturated sandstone samples, finding $0.25 < Z_N/Z_T < 3$ when the samples were dry and that water saturation reduced Z_N/Z_T to $0.05 < Z_N/Z_T < 1.1$. As well as investigating sandstones, Sayers (1999) investigated the Z_N/Z_T ratio in shale samples. Sayers (1999) inverted ultrasonic measurements made by Johnston and Christensen (1993) on dry shale samples and by Hornby (1994) on saturated shale samples finding that $0.47 < Z_N/Z_T < 0.8$ in dry shale samples and $0.26 < Z_N/Z_T < 0.41$ in water-saturated shale samples.

MacBeth and Schuett (2007) used ultrasonic data to measure Z_N/Z_T on initially undamaged core samples and then on the same samples after they had been damaged by heating, creating intra- and intergranular fractures. MacBeth and Schuett (2007) found that the initial samples have $0 < Z_N/Z_T < 0.6$, while after heating and damage, $0 < Z_N/Z_T < 1.2$. MacBeth and Schuett (2007) noted that pre-existing micro-fractures in the initial sample had experienced diagenetic infill, while the new micro-fractures created by thermal treatment had smoother faces and were unfilled. These differences were inferred to be the reason for the increase in Z_N/Z_T caused by heating damage.

Hsu and Schoenberg (1993) developed a method to create synthetic, representative samples. By compressing

together roughened Perspex plates, they created samples containing discontinuities that replicated fractures. The advantage of constructing synthetic samples is that the geometry, distribution and properties of the fractures should be well constrained *a priori*, allowing observations to be directly attributed to these properties. Hsu and Schoenberg (1993) imaged their samples with ultrasonic measurements, finding $0.8 < Z_N/Z_T < 1$ in dry conditions. Hsu and Schoenberg (1993) investigated the effects of fluid saturation on Z_N/Z_T, finding that saturating the samples with honey reduced Z_N/Z_T to 0.1.

An alternative method to create a synthetic sample was developed by Rathore *et al.* (1994), who constructed a synthetically fractured rock with a known distribution of cracks. The sample was created by cementing sand with epoxy resin. Included in the sample were metal discs to create discontinuities – the discs were removed after the sample had been constructed by a chemical leaching agent, leaving behind a known distribution of crack-like voids. Ultrasonic P- and S-wave velocities were then measured at a range of angles to the fracture set. Rathore *et al.* (1994) did not compute Z_N/Z_T, however it can be determined using their ultrasonic data. Hudson, Pointer and Liu (2001) used the frequency-dependent crack model of Hudson *et al.* (1996a) to fit Rathore *et al.*'s (1994) results. We used the best-fit parameters that Hudson *et al.* (2001) computed (specifically Matrix A in Table 3 of Hudson *et al.* 2001) to derive a value for Z_N/Z_T of 0.46.

Pyrak-Nolte *et al.* (1990) used ultrasonic data to measure the compliance of a single fracture running through a core sample of quartz monzonite. Such an experiment is probably more representative of larger-scale fractures in rocks (rather than the grain-scale fabrics measured by Sayers 1999; Sayers and Han 2002; MacBeth and Schuett 2007; Verdon *et al.* 2008 and Angus *et al.* 2009, or synthetic samples created by Hsu and Schoenberg 1993 and Rathore *et al.* 1994). Pyrak-Nolte *et al.* (1990) found $0.20 < Z_N/Z_T < 0.77$ for dry samples. Saturating the samples with water reduced Z_N/Z_T to $0.04 < Z_N/Z_T < 0.48$. Similarly, Lubbe *et al.* (2008) cut and then reassembled limestone core samples to create samples with a single fracture, which were imaged using ultrasonic data, finding $0.20 < Z_N/Z_T < 0.55$. Saturation of the fractures with honey produced a dramatic reduction in Z_N/Z_T to $0.02 < Z_N/Z_T < 0.05$.

A number of generalizations can be made from these results. Firstly, changing the fluid saturating the fractures alters Z_N/Z_T. Whether the saturating fluid was water or honey, Sayers (1999), Hsu and Schoenberg (1993), Sayers and Han (2002), Pyrak-Nolte *et al.* (1990) and Lubbe *et al.* (2008) all found that the presence of a stiff fluid significantly reduced Z_N/Z_T from the dry, unsaturated cases. Secondly, the internal architecture of the fractures also influences Z_N/Z_T. MacBeth and Schuett (2007) noted differences in the diagentic infill between pre-existing micro-fractures and those created by thermal damage, where Z_N/Z_T had increased significantly. Specifically, the newly created micro-fractures had cleaner, smoother faces and no cementation. However, while it is clear that observed variations in Z_N/Z_T are caused by changes in fracture architecture, characterizing the changes and formulating rules-of-thumb that can be used to interpret field data remain a greater challenge than variations produced by changes in fluid saturation. Broadly, however, we conclude that the generalizations made from experimental observations appear to support the rock physics models discussed above.

Finally, the issue of upscaling laboratory measurements, usually made at ultrasonic frequencies on centimetre-scale samples, to metre-scale fractures imaged with decametre-scale seismic waves, must be addressed. We are aware of only one field-scale measurement of Z_N/Z_T: Hobday and Worthington (2012) used hammer seismics to image Z_N/Z_T of a water-saturated outcrop of Upper Caithness Flagstone, finding that $Z_N/Z_T \leq 0.1$. With only one field-scale measurement, it is difficult to draw any inferences about upscaling. Therefore, the approach developed in this paper to image Z_N/Z_T using downhole microseismic data should help produce additional field-scale data to address this issue.

Measurement of Z_N/Z_T during hydraulic fracture stimulation: 'beyond the dots in the box'

Production from tight and shale gas reservoirs is experiencing a dramatic increase (e.g., Jacoby, O'Sullivan and Paltsev 2012). Such reservoirs require either pre-existing natural fractures or hydraulic fracture stimulation (or both) to produce at economic rates. As a result, the use of microseismic monitoring to image fractures during stimulation has expanded significantly (e.g., Maxwell 2010). However, there is currently a push to derive more information from microseismic monitoring of hydraulic fracture stimulations than the fracture geometry as revealed by event hypocentre locations – to go 'beyond the dots in the box' (Eisner *et al.* 2010). The rock physics models and experimental observations discussed above suggest that measurement of the Z_N/Z_T ratio of the fractures in a reservoir has the potential to (1) identify the bulk modulus of the fluid filling the fractures (in particular discriminating between water or gas filled), (2) to determine the ability of fluids to flow

between fractures and the rock porosity and (3) to discriminate between 'older', possibly diagenetically affected fractures and newly-created, smooth fractures, or indeed fractures filled with proppant. All of the above will have a direct influence on the fluid-flow properties of the fractures. Therefore, as well as helping to constrain Z_N/Z_T for future waveform modelling studies (e.g., Vlastos *et al.* 2006; Sayers and den Boer 2012) a technique capable of measuring the Z_N/Z_T ratio of fractures during hydraulic stimulation will be a valuable tool that allows geophysicists to provide a greater degree of information to reservoir engineers than the fracture length and orientation as provided by microseismic event locations.

INVERTING FOR Z_N/Z_T USING S-WAVE SPLITTING MEASUREMENTS

Seismic anisotropy is the directional dependence of seismic wavespeed. In hydrocarbon reservoirs, the most significant causes of anisotropy are sedimentary fabrics, which are usually orientated sub-horizontally and sets of aligned fractures, which are usually orientated subvertically. Seismic anisotropy can be imaged with a number of observations, such as azimuthal variation in reflection amplitudes (e.g., Hall and Kendall 2000) and interval normal moveout velocities from reflection seismic surveys. However, the most unambiguous indicator of seismic anisotropy is S-wave splitting. When an S-wave enters an anisotropic region, it is split into two orthogonally waves with different speeds. The polarization of the faster wave (ψ) and the time lag between arrivals (δt) can be measured on a three-component geophone using an automated approach (Wüstefeld *et al.* 2010). The time lag is normalized by path length to give the percentage velocity difference between fast and slow S-waves (δV_S). Verdon and Kendall (2011) and Wüstefeld *et al.* (2011a,b) showed how microseismic events detected on downhole, three component geophones provide an ideal opportunity to image anisotropic fabrics using SWS.

Using equations (1) and (2), it is possible to compute the compliance tensor for a rock containing a vertical, aligned fracture set with a pre-defined Z_N/Z_T ratio. To model the SWS for the fractured rock, we invert the compliance to give the stiffness tensor $\mathbf{C}$ ($\mathbf{C} = \mathbf{S}^{-1}$). $\mathbf{C}$ is then used in the Christoffel equation to compute the velocities and polarizations of the three body waves (quasi-P, fast S, slow S) that propagate through an anisotropic rock, from which the SWS operators, ψ and δV_S, are calculated. Figure 2 shows upper hemisphere projections of the modelled P-wave velocity and SWS for a vertical fracture set with strike of 70° and $Z_N/Z_T = 0.1$ or $Z_N/Z_T = 0.9$. These figures show the influence of Z_N/Z_T on seismic velocities. For S-wave propagation parallel to the fractures (both vertically and/or parallel to fracture strike), ψ is parallel to the fracture strike and δV_S is controlled by Z_T and so is unaffected by Z_N/Z_T. However, for S-waves propagating at oblique angles to the fracture set, both ψ and δV_S are affected by Z_N/Z_T. This sensitivity allows us to image the Z_N/Z_T ratio of an aligned set of fractures using SWS measurements made on microseismic data.

In this paper we make an extension to the inversion method developed in Verdon *et al.* (2009), allowing as an additional degree of freedom the Z_N/Z_T ratio, where previously (Verdon *et al.* 2009; Verdon and Kendall 2011; Wüstefeld *et al.* 2011a,b) it was fixed according to the relationship given in equation (3). The objective function to be minimized by the inversion is the misfit between the measured and modelled SWS operators (ψ and δV_S) for the observed S-wave arrivals. To model the SWS for a given fracture strike, Z_N and Z_T we use the approach outlined in equations (1) and (2) to compute the stiffness tensor. The SWS operators for each given arrival azimuth and inclination are then calculated using the Christoffel equation.

As well as fracture properties, Thomsen's (1986) parameters are used to assign a VTI fabric to the compliance of intact, unfractured rock ($\mathbf{S}^{\mathrm{r}}$), such as might be produced by sedimentary layering (e.g., Backus 1962) and alignment of phyllosilicate minerals (e.g., Valcke *et al.* 2006; Hall *et al.* 2008). Error analysis (Wüstefeld *et al.* 2011b) has shown that, with only SWS data and no P-wave information, Thomsen's ϵ and δ parameters cannot be constrained, as they trade-off against each other. Nevertheless, they are both included as free parameters in the inversion.

The free parameters in the inversion are therefore Thomsen's ϵ, γ and δ parameters, fracture strike, the tangential compliance, Z_T and the ratio of normal to tangential compliance, Z_N/Z_T. The additional parameters in the inversion makes a grid search approach (as used by Verdon and Kendall 2011) impractical. Instead, we use the Neighbourhood Algorithm approach (Sambridge 1999a) to search the parameter space for the best fitting rock physics model and Bayesian integration to assess the statistical significance of the resulting ensemble of models (Sambridge 1999b).

THE COTTON VALLEY S-WAVE SPLITTING DATA SET

In this paper we demonstrate our inversion for Z_N/Z_T using SWS measurements made on microseismic data

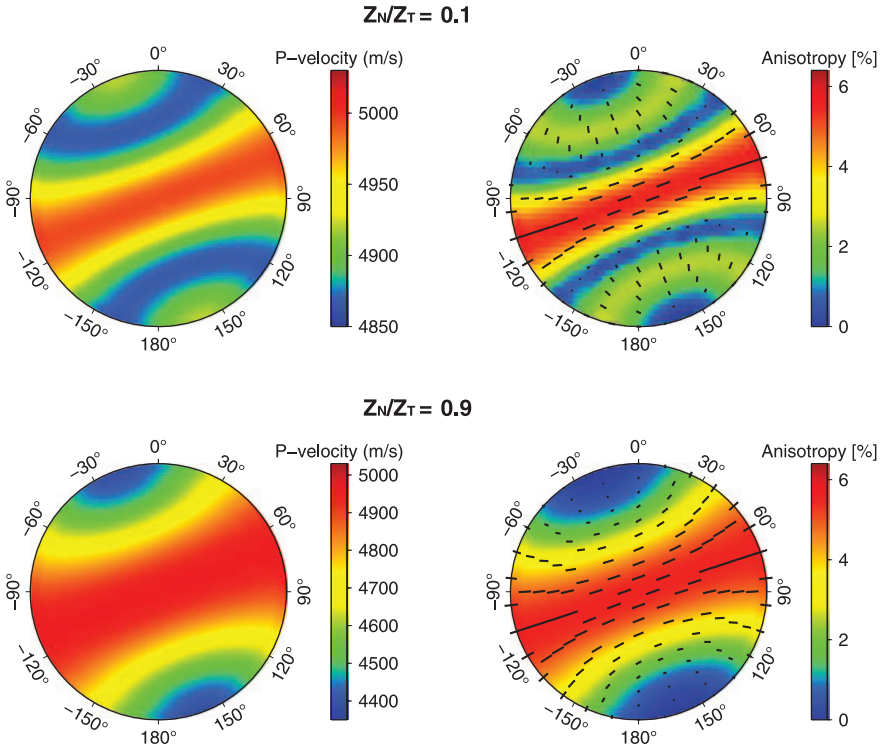

Figure 2 Upper hemisphere projections of phase velocities as a function of propagation direction through a rock mass containing a single set of fractures striking at 70°, with fracture density of 0.05 and $Z_N/Z_T = 0.1$ (top) and $Z_N/Z_T = 0.9$ (bottom). Left-hand plots show P-wave velocities – velocities are fastest when propagating parallel to the fracture set (either vertically or horizontally at 70°). Right-hand images show SWS magnitude, δV_S (contours and tick lengths) and fast wave polarization, ψ (tick orientation). Note the differences in both ψ and δV_S for S-waves travelling at oblique angles to the fracture set.

collected during hydraulic fracture stimulation at Cotton Valley, East Texas (Walker 1997; Urbancic and Rutledge 2000). The Cotton Valley formation consists of sandstones interbedded with shale and carbonate horizons over a thickness of 325 m. The low permeability of the formation requires hydraulic fracturing for economic production. SWS measurements were made on microseismic data collected on downhole geophone arrays during one stage (so-called 'Treatment B')

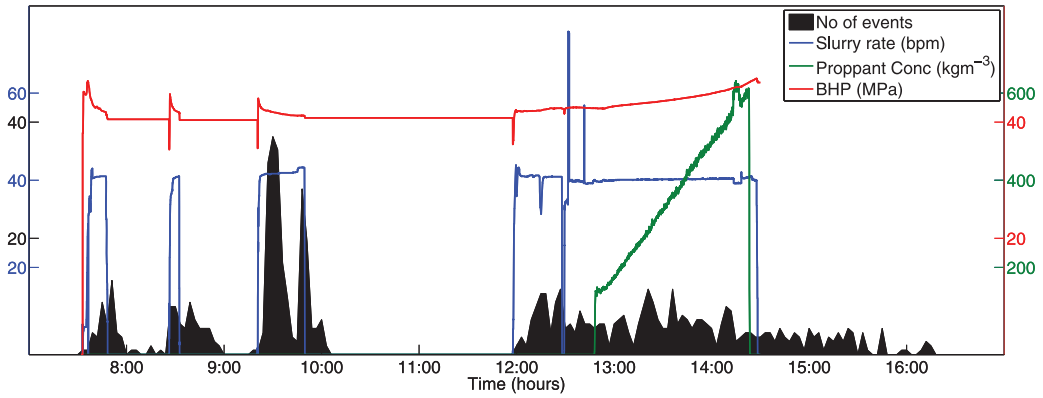

Figure 3 Slurry injection rates (blue), proppant concentration (green), bottom-hole pressure (red) and rate of microseismicity (black shaded area) during Cotton Valley Treatment 'B'. Slurry injection occurs in three separate phases, before a final phase during which proppant is also introduced. Seismicity is observed during each phase, peaking during the 3rd slurry injection phase.

of a fracture stimulation described in Rutledge and Phillips (2003) and Rutledge, Phillips and Mayerhofer (2004). The rates of slurry injection, proppant concentration, the bottom-hole pressure and the rate of induced microseismicity during this treatment are plotted in Fig. 3. Slurry is injected in three initial phases, before a final phase during which proppant is also introduced. Seismicity occurs during each injection phase, peaking during the 3rd injection phase.

Microseismic events were recorded on two downhole geophone arrays. The locations of both events and geophones are plotted in Fig. 4. During injection, events initiate at the injection point and extend laterally along an ENE-WSW trend. A total of ~900 events were detected during this treatment. Both focal mechanism analysis (Rutledge *et al.* 2004) and SWS measurements (Wüstefeld *et al.* 2011b) have shown how the trend of the hydraulic fracturing, at 80°, interacts with a natural fracture set that has a strike of 70°.

SWS measurements were performed on the Cotton Valley microseismic data using an automated algorithm (Wüstefeld *et al.* 2010) and were presented in Wüstefeld *et al.* (2011b). Of the 18 000 possible SWS measurements (900 events × 20 geophones), a total of 1545 yielded measurements of the highest quality (as defined by Wüstefeld *et al.* 2010), a typical rate of return for SWS studies.

S-wave splitting is a path-averaged effect, meaning that the observed measurement is a function of all of the rock through which the wave has propagated, from source to geophone. Therefore, an assumption implicit in this approach is that the anisotropy system is relatively homogenous between sources and geophone (Verdon *et al.* 2009). The geophones at Cotton Valley are sited both in the top layers of the Cotton Valley Formation and in the overlying Travis Peak Formation, a similar low-permeability sand and mudstone sequence. Without *a priori* measurements of the anisotropy of these formations, it is difficult to assess whether the assumption of relatively homogenous anisotropy is met. Perhaps the best indication of the suitability of this assumption is that, when inverting the measured SWS data for fracture properties, our best fitting models provide a good match with the observations. Where significant spatial variations in seismic anisotropy are present, tomographic methods (e.g., Wookey 2012) are required to fit the resulting SWS measurements. Furthermore, we are generally most interested in temporal variations in SWS during the fracture stimulation. Inasmuch as the only process occurring in the vicinity during the period of interest was the fracture stimulation itself, it can be safely assumed that any temporal variations that are observed are due to processes occurring in and around the fracture stimulation.

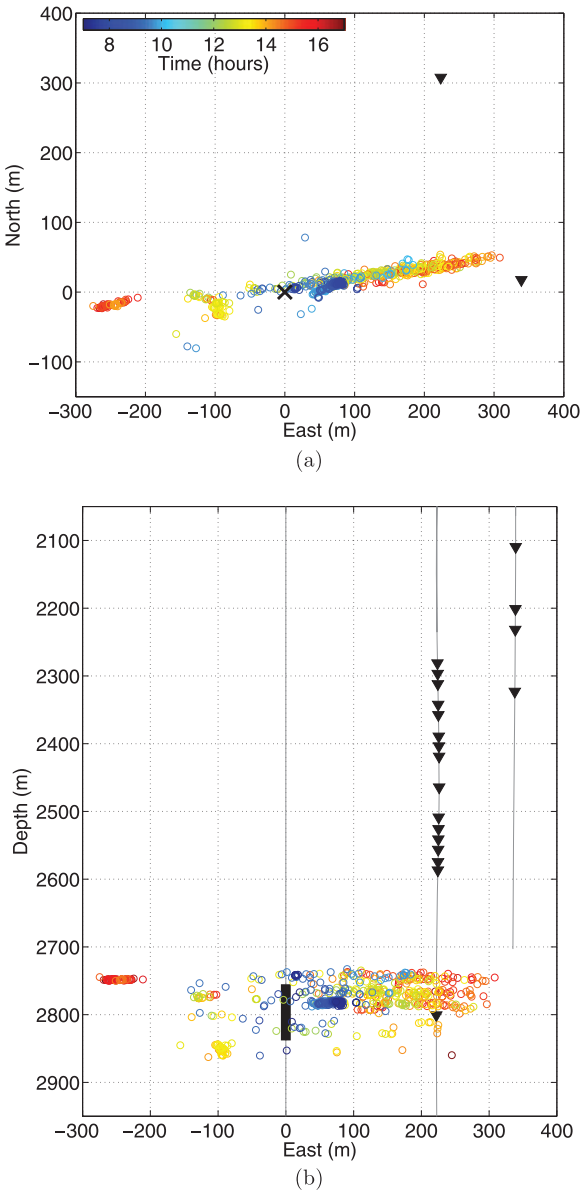

Figure 4 Map view (a) and cross-section (b) showing event locations (circles) and monitoring geophones (black triangles) during Treatment 'B'. In (a) the injection well is marked by a black ×, in (b) the injection interval is marked by the thick black line. The event locations are coloured by occurrence time. The events initiate at the injection point and extend laterally with an ENE-WSW trend.

ERROR ANALYSIS

Verdon *et al.* (2009) showed how the ability of the inversion process to image fractures is dependent on the aperture of arrival angles provided by the observed S-waves. Therefore, before inverting the observed SWS measurements, we conduct a synthetic test to confirm that the range of illumination

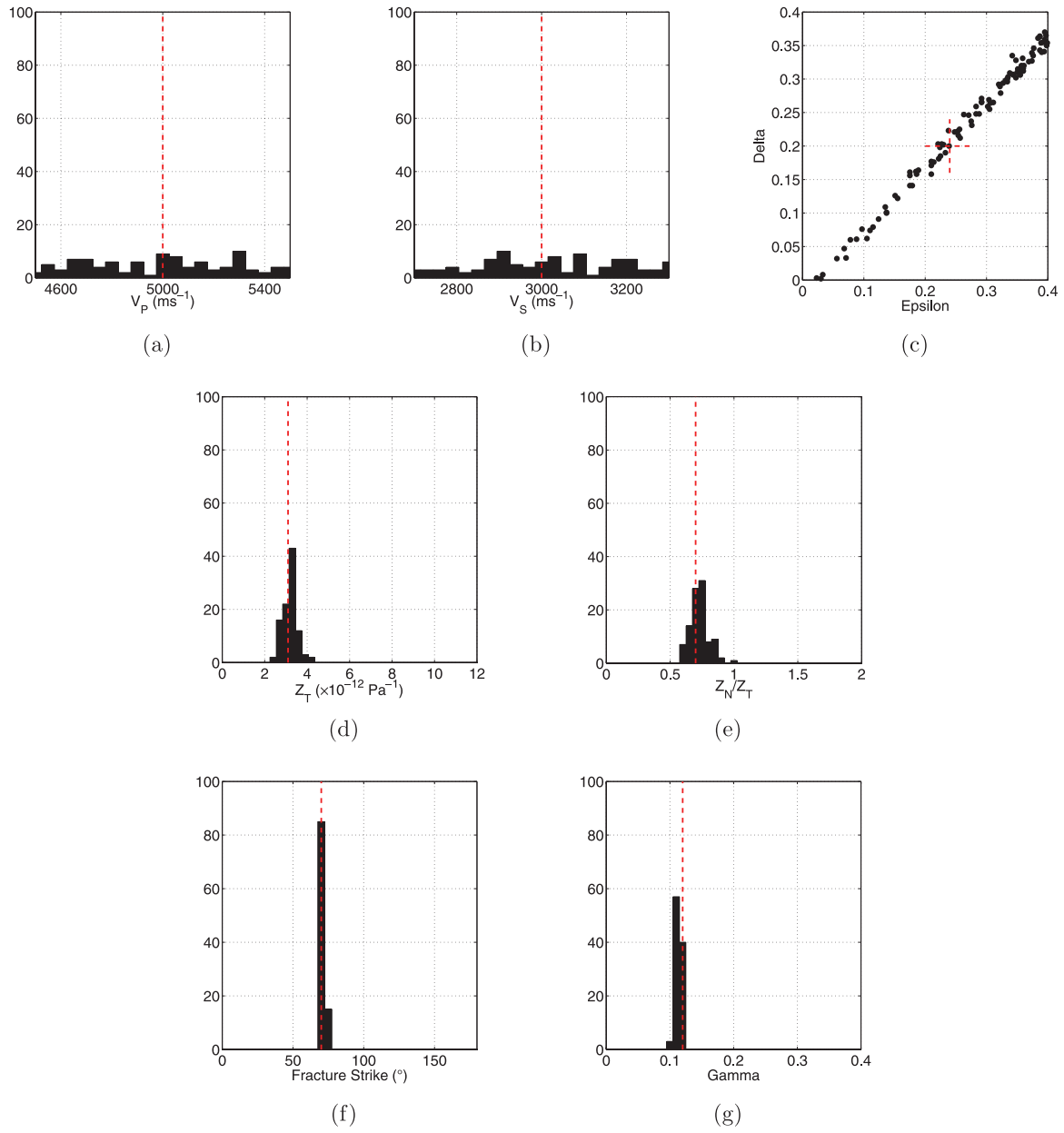

Figure 5 Results of the error analysis to test the ability of the inversion to return accurate values of Z_N/Z_T. Panels (a) and (b) show histograms of the erroneous values of V_P and V_S used in the inversion. Panel (c) shows the recovered values of ϵ and δ, highlighting the trade-off introduced by a lack of P-wave information, which means that neither parameter is well constrained. Panels (d–g) show histograms of the values of Z_T, Z_N/Z_T, fracture strike and γ recovered by the inversion. The red dashed lines show the parameters used to generate the initial model. Both Z_T and Z_N/Z_T are accurately recovered. The degree of spread gives an assessment of the degree of error when inverting the measured data.

angles provided by the Cotton Valley SWS data is sufficient to image Z_N/Z_T accurately. To do so we construct an initial model with $Z_N/Z_T = 0.7$, $Z_T = 3 \times 10^{-12}\text{Pa}^{-1}$, fracture strike $= 70^\circ$ and Thomsen's parameters of $\epsilon = 0.24$, $\gamma = 0.12$ and $\delta = 0.2$. The SWS operators (ψ and δV_S) were computed for a randomly selected subset of 150 of the 1500 S-wave arrivals measured at Cotton Valley. Noise was added to these modelled values, with a random distribution of $\pm 10^\circ$ to the observed arrival azimuth and inclination (representing errors in event location) and $\pm 10^\circ$ to ψ and $\pm 0.5\%$ to δV_S (representing errors in SWS measurement). Also, random noise of $\pm 10\%$ was added to the background P- and S-wave velocities

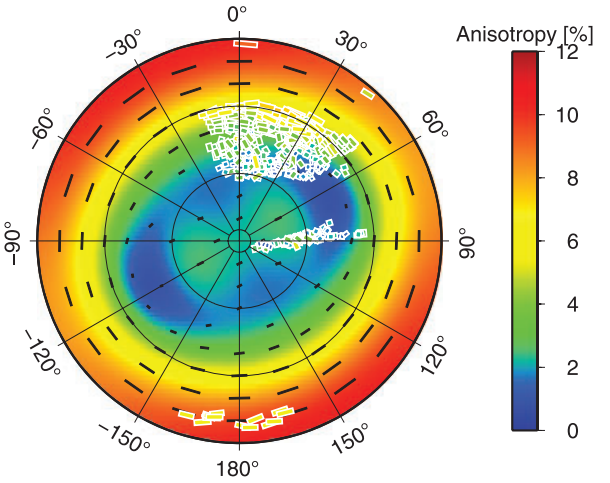

Figure 6 Polar projection of measured SWS data (white outlined ticks) and best fitting model (black ticks and contours). Tick locations show the arrival azimuths and inclinations of incoming S-waves. Tick orientations show the polarization direction of the fast S-wave, tick lengths and colours show the magnitude of splitting.

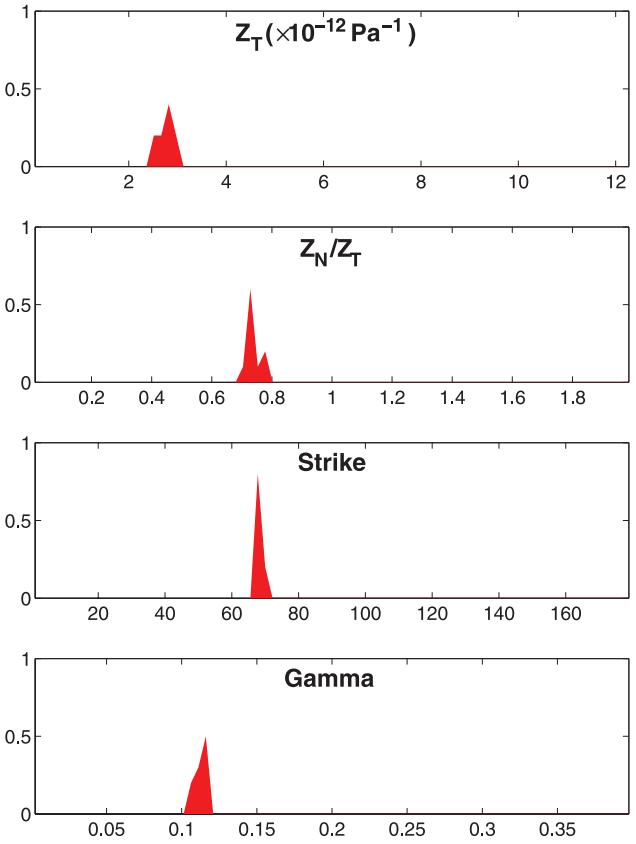

Figure 7 Normalized posterior probability distributions (Sambridge 1999b) for the inversion parameters Z_T, Z_N/Z_T, fracture strike and Thomsen's γ parameter. All parameters are well constrained by the inversion.

used in the inversion, representing potential velocity model errors. These noisy synthetic data were then re-inverted to recover the initial parameters.

This procedure – random selection of S-wave arrival angles, forward modelling of SWS, addition of noise, inversion using erroneous values of V_P and V_S – was repeated 100 times. The ability (or inability) of the inversion to recover the initial values of Z_T and Z_N/Z_T will show how well the inversion results can be constrained. The results of the synthetic error analysis are shown in Fig. 5. Figure 5(a,b) shows the erroneous values of V_P and V_S used as input for the inversion. Figure 5(c) shows the recovered values of ϵ and δ. Without P-wave data, these values trade-off against each other and cannot be constrained. Figure 5(d–g) shows the values of Z_T and Z_N/Z_T, fracture strike and γ recovered by the synthetic inversion. We note that all of the parameters were well recovered, implying that we can have confidence in the inversion results when using real SWS measurements from Cotton Valley.

RESULTS

We begin by inverting the full data set of SWS measurements. Figure 6 shows the SWS measurements overlain on the SWS predicted by the best-fit model. A good match between observed and modelled splitting operators is noted. The posterior probability distributions for each parameter, as computed by Bayesian integration (Sambridge 1999b), are plotted in Fig. 7. The parameters of the best-fit model, as well as the 95% confidence limits, are listed in Table 2. The inversion returns a fracture strike of 68°, which matches the value found by Wüstefeld *et al.* (2011b) (who assumed scalar fractures). The value of γ returned is 0.11, also in agreement with Wüstefeld *et al.* (2011b). A value of $2.71 \times 10^{-12}\text{Pa}^{-1}$ is returned for Z_T and $Z_N/Z_T = 0.74$. The significance of these results will be considered further in the discussion section.

Spatial and temporal variation of Z_N/Z_T

Observations of temporal variations in SWS have been useful in imaging changes in fracturing through time (e.g., Crampin, Volti and Stefánsson 1999; Teanby, Kendall and van der Baan 2004; Wüstefeld *et al.* 2011a,b). As well as inverting the full data set, we can use our inversion technique to image temporal changes in Z_N/Z_T during the fracture stimulation. A sliding time window is applied to the data, dividing the injection period into 6-minute bins. For each bin, all SWS measurements

within ±15 minutes are utilized in the inversion (with the additional stipulation of a minimum of 10 events per bin). The resulting temporal variations in Z_N, Z_N/Z_T, fracture strike and Thomsen's γ parameter are shown in Fig. 8, alongside the injection rate and seismicity data. We note that variations in strike and γ are notably lower than variations in Z_N/Z_T. This might be expected as fracture stimulation should not affect the strength of intrinsic anisotropy caused by sedimentary fabrics, or the strike of pre-existing fracture sets.

Wüstefeld *et al.* (2011b) noted an increase in fracture density with time during the stimulation, most notably at the end of the stage when proppant is introduced. Figure 8 shows that Z_T is in fact reasonably constant throughout the stage, while Z_N/Z_T and by extension Z_N, increase both during the 2nd injection stage and, most notably, during the final stage. The increase in Z_N/Z_T during the final stage is contemporaneous with proppant injection.

Event hypocentre locations move away from the injection point during the injection period (Fig. 4). Therefore it is possible that apparent temporal variations are in fact produced by spatial variations. This entanglement of spatial and temporal variation is inherent to many SWS experiments: are observed changes due to heterogeneity, or temporal changes produced by the fracturing process? Wüstefeld *et al.* (2011b) addressed this issue for the Cotton Valley SWS data, studying in detail the S-wave splitting from events located closely together. They found significant changes in SWS through time that could not be explained by spatial variation, as the event locations were too close. Therefore they favoured the interpretation that observed SWS changes were produced by the processes of hydraulic fracturing, rather than any pre-existing heterogeneity. Given that hydraulic fracturing, by its very nature, will be creating new fractures and altering the properties of pre-existing fractures, it is not surprising that these changes should produce temporal SWS variations.

In Fig. 9 we examine the spatial and temporal variations in Z_N/Z_T in more detail. This plot shows hypocentres and occurrence times for each event. As the temporal windows used to generate Fig. 8 overlap, SWS observations from each event will have been used several times to invert values of Z_N/Z_T. Each window (i.e., each data point in Fig. 8) has a width of 30 minutes, shifted by 6 minutes for each window (so window

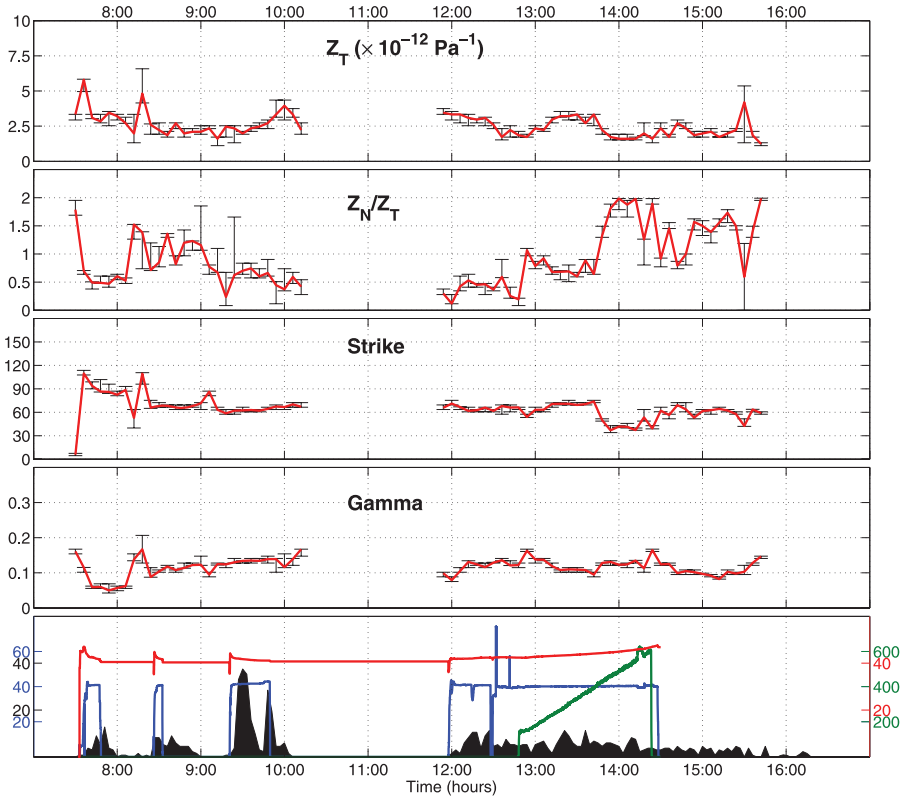

Figure 8 Temporal variation of inversion parameters (Z_T, Z_N/Z_T, fracture strike, Thomsen's γ) during the injection stage. The lowermost panel shows seismicity and injection data (for legend see Fig. 3).

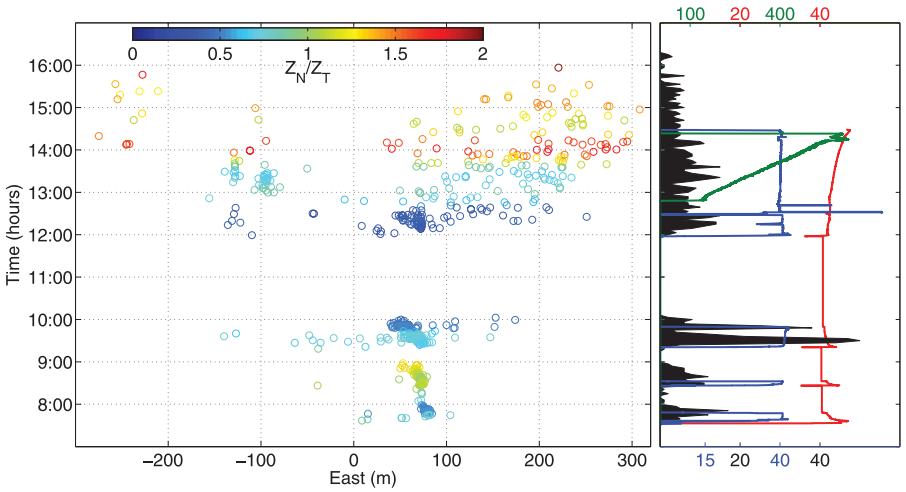

Figure 9 Spatial and temporal variation of Z_N/Z_T. Each dot represents an event hypocentre (easting coordinate) and occurrence time. Events initiate around the injection point (easting of 0) and extend outwards through time. The changes in Z_N/Z_T are dominated by temporal variations. The right-hand panel shows seismicity and injection data (for legend see Fig. 3).

1 contains all SWS measurements between 7:30 ± 15 minutes, window 2 between 7:36±15 minutes and so on), meaning that SWS measurements from each event will have been used by 5 inversions for temporal variations in Z_N/Z_T. In Fig. 9, each event is coloured according to the average inverted Z_N/Z_T ratio generated from the SWS measurements for that particular event. Figure 9 implies that temporal variations dominate the observed variations in Z_N/Z_T. Events in similar locations return different values for Z_N/Z_T depending on occurrence time. This is most notable for events between 12:00 to 16:00 – there is little notable variation in the spatial distribution of events used in the inversions, yet Z_N/Z_T changes significantly. As mentioned previously, this change correlates with the introduction of proppant.

In the following discussion section we outline the potential causes of this temporal variation in Z_N/Z_T, using the experimental observations summarized in Table 1 and Fig. 1 as a framework for our interpretations. Given our current limited understanding of the controls on Z_N/Z_T, reaching an unambiguous interpretation may be challenging. We note here that the key finding of this paper is that SWS measurements on microseismic data render such observations possible. We anticipate that further measurements of Z_N/Z_T using more hydraulic stimulation data sets, presented in conjunction with other advanced microseismic imaging techniques, such as source mechanism inversion (e.g., Nolen-Hoeksema and Ruff 2001) and/or calculation of the seismic *b*-value (e.g., Wessels *et al.* 2011), will provide a greater understanding of how the hydraulic fracture stimulation process affects Z_N/Z_T and therefore how such measurements can be used to provide useful information to reservoir engineers.

DISCUSSION

Z_N/Z_T ratio

Table 1 lists published ranges for Z_N/Z_T measured using a number of techniques, including: ultrasonic laboratory measurements made on both fractured and undamaged core samples (Sayers 1999; Sayers and Han 2002; MacBeth and Schuett 2007; Verdon *et al.* 2008; Angus *et al.* 2009); laboratory measurements on core samples containing a single fracture (Pyrak-Nolte *et al.* 1990; Lubbe *et al.* 2008); synthetic representative samples constructed using Perspex plates (Hsu and Schoenberg 1993) or sand cemented by epoxy resin (Rathore *et al.* 1994); and finally seismic measurements on fractures in the field (Hobday and Worthington 2012). These studies found Z_N/Z_T varying from 0–3. Inverting the full Cotton Valley SWS data set gives a value of $0.7 < Z_N/Z_T < 0.78$.

Given the scarcity of field measurements of Z_N/Z_T in the literature, it is instructive to compare our results with the field measurements of Hobday and Worthington (2012), who found that $Z_N/Z_T \leq 0.1$ for a water-saturated outcrop of Caithness sandstone. Our value of Z_N/Z_T is significantly larger. A key difference that might account for this discrepancy is that, while Hobday and Worthington's (2012) measurements are of water-saturated fractures, our measurements

are made in a gas reservoir. Rock physics theory predicts that water, as a stiffer fluid, can serve to stiffen fractures, lessening Z_N, an effect much reduced for fractures saturated with gas, which is more compliant. Pyrak-Nolte *et al.* (1990), Hsu and Schoenberg (1993) and Lubbe *et al.* (2008) all note a reduced Z_N/Z_T for water and/or honey saturated fractures. As we have seen, both rock physics modelling and experimental observations have shown that saturation of fractures by water will reduce Z_N/Z_T.

However, we observe a significant variation in Z_N/Z_T during the fracture stimulation (Fig. 8). It is unlikely that fluid substitution is alone responsible for these variations. During the proppant injection phase, Z_N/Z_T increases to values between $1 < Z_N/Z_T < 2$. This is higher than most experimental and theoretical values for Z_N/Z_T available in the literature. We note the experimental work of MacBeth and Schuett (2007), where the creation of new, clean fractures produced an increase in Z_N/Z_T. Previous work Rutledge *et al.* (2004) has shown how the stimulation at Cotton Valley combines re-activiation of pre-existing fractures with newly created hydraulic fractures. It is possible that the observed increase in Z_N/Z_T corresponds to a point where the creation of new fractures begins to dominate the process.

Our interpretations must be considered tentative at this stage. It is notable that the increase in Z_N/Z_T is contemporaneous with proppant injection. The effects that the presence of proppant will have on the compliance ratio of fractures is as yet unknown. Therefore, it is feasible that the observed Z_N/Z_T increase might be a direct indication of proppant in the fractures. Another potential cause is that an increase in rock permeability or fracture connectivity will increase the rate of fluid exchange between fractures, and between fractures and the rock porosity, meaning that the fractures will appear to behave in a 'drained' manner, increasing Z_N/Z_T (e.g., Hudson *et al.* 1996a; Pointer *et al.* 2000; Chapman 2003).

This paper represents the first measurement of Z_N/Z_T during hydraulic fracture stimulation. Further measurements of Z_N/Z_T on the ever-increasing number of hydraulic fracturing data sets, alongside modelling and experimental studies to determine the factors that influence Z_N/Z_T, will allow observations of Z_N/Z_T during hydraulic fracturing to be interpreted with a greater degree of confidence.

Compliance and fracture length

Our inversion returns absolute values for the compliance of fractures, Z_N and Z_T (as well as the ratio Z_N/Z_T). It is instructive to consider how our results compare with published values of fracture compliance. Worthington (2007) and Worthington and Lubbe (2007) noted a scaling of fracture compliance with fracture length. In Fig. 10 we plot our results alongside the data compiled by Worthington and Lubbe (2007). In this figure, the ordinate axis is the compliance of an individual fracture ($B_{N,T}$) with units mPa^{-1}. To convert our results, which give the compliance of the overall fracture set, with units of Pa^{-1}, we use the relationship cited by Hobday and Worthington (2012),

$$B_{T,N} = LZ_{T,N}, \tag{4}$$

where L is the fracture spacing. Laubach (1988) and Laubach and Monson (1988) made estimates of fracture length and spacing at Cotton Valley using core samples and borehole logs. They placed a minimum bound on the spacing of natural fractures at 10 cm. Therefore, following as an example the treatment of Herwanger *et al.* (2004) by Worthington and Lubbe (2007), we set bounds on the fracture spacing of between 1 fracture/metre to 10 fractures/metre. The resulting range of B_T values are $2.47\times\ 10^{-13}$ to $2.96\times\ 10^{-12}\mathrm{mPa}^{-1}$. These values are plotted in Fig. 10, along with the data reported by Worthington and Lubbe (2007). Although information on fracture length is limited, Laubach (1988) suggested a maximum fracture length of 2.5 m. In Fig. 10 our results are plotted at this value for fracture length scale.

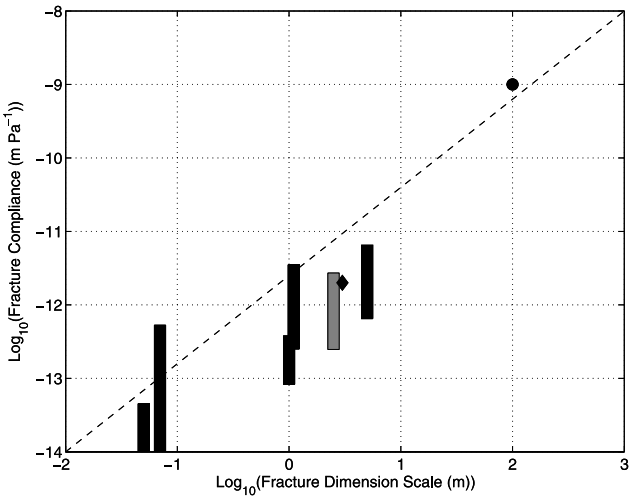

Figure 10 Fracture compliance as a function of fracture length scale (Worthington and Lubbe 2007). Worthington and Lubbe's (2007) data are plotted in black, the results from this study are represented by the gray bar, plotted at the maximum bound for fracture length (2.5 m). Our data fall within the range of Worthington and Lubbe's (2007) collated data. We therefore infer bounds of fracture length scale of between 0.5–10 m.

Table 1 Published measurements of Z_N/Z_T from both laboratory and field studies.

	Reference	Notes	$>Z_N/Z_T$
1	Verdon *et al.* (2008)	Dry samples. Ultrasonic measurement on grain-scale fabrics. Data from Hall *et al.* (2008)	0.68–1.06
2	Angus *et al.* (2009)	Dry samples. Ultrasonic measurement on grain-scale fabrics. Data collated from a range of literature sources.	0.25–1.5
3(a)	Sayers and Han (2002)	Dry samples. Ultrasonic measurement on grain-scale fabrics. Data from Han *et al.* (1986)	0.25–3
3(b)		As above, water saturated.	0.05–1.1
4(a)	Sayers (1999)	Dry samples. Ultrasonic measurement on shale samples. Data from Johnston and Christensen (1993) and Vernik (1993)	0.47–0.8
4(b)		As above, water saturated. Data from Hornby (1994)	0.26–0.41
5(a)	MacBeth and Schuett (2007)	Dry samples. Ultrasonic measurement on grain-scale fabrics. Undamaged sample.	0–0.6
5(b)		As above, sample thermally damaged.	0–1.2
6(a)	Hsu and Schoenberg (1993)	Representative medium of compressed perspex plates. Ultrasonic measurements on dry samples.	0.8–1
6(b)		As above, honey saturated.	0.1
7	Rathore *et al.* (1994)	Synthetic sample containing a population of cracks. Ultrasonic data reanalysed by Hudson *et al.* (2001).	0.46
8(a)	Pyrak-Nolte *et al.* (1990)	Quartz monzonite samples containing a single fracture. Ultrasonic measurements on dry samples.	0.2–0.7
8(b)		As above, water saturated.	0.04–0.5
9(a)	Lubbe *et al.* (2008)	Limestone samples cut and reassembled to create a single fracture. Ultrasonic measurements on dry samples.	0.2–0.55
9(b)		As above, honey saturated.	0.02–0.05
10	Hobday and Worthington (2012)	Hammer seismic imaging of outcrop of Caithness Flagstone. Water saturated	$\leq$0.1

Our data fall within the range of data collated by Worthington and Lubbe (2007). We use the linear relationship derived by Worthington and Lubbe (2007) (black dashed line in Fig. 10) and, noting that this relationship appears to underestimate fracture length scale for measurements of $\sim$1 to 10 m, infer bounds on the fracture length scale at Cotton Valley of 0.5–10 m. Our interpolated bounds, computed by inversion of SWS measurements, match well with the estimates of fracture length scale made by Laubach (1988) and Laubach and Monson (1988) from core samples and borehole logs. We conclude that our data appear to support the conclusions made by Worthington and Lubbe (2007) regarding the scaling of fracture compliance.

CONCLUSIONS

We developed a method to invert SWS measurements made on microseismic data for the ratio of normal and tangential compliances of aligned fracture sets (Z_N/Z_T). We demonstrated our technique by inverting microseismic data from a Cotton Valley hydraulic fracture stimulation. Before inverting the SWS measurements, a synthetic data set was generated and inverted in order to test the resolution of the inversion method. This synthetic test indicated that it should be possible to constrain Z_N/Z_T using SWS data measured on microseismic data.

Inversion of the full Cotton Valley SWS data set revealed $Z_N/Z_T = 0.74 \pm 0.4$. Windowing the data by time revealed significant temporal variations in Z_N/Z_T. Experimental

Table 2 Inversion results for the full data set. Without P-wave data, ϵ and δ cannot be constrained.

	$Z_T(\times 10^{-12}\mathrm{Pa}^{-1})$	Z_N/Z_T	*Strike* (°)	ϵ	γ	δ
Best-fit result	2.71	0.74	68	NA	0.11	NA
95% limits	2.47–2.96	0.7–0.78	67–70	NA	0.10–0.12	NA

observations and rock physics models indicated that Z_N/Z_T will be sensitive to the stiffness of the fluid that is filling the fractures, as well as the roughness of the fracture faces and the presence of diagenetic material, or proppant, filling the fractures. The most significant temporal variation we observe is an increase in Z_N/Z_T that is contemporaneous with proppant introduction. A number of mechanisms have the potential to raise Z_N/Z_T during stimulation, including the formation of new, clean fractures, or an increase in fracture connectivity that promotes 'drained' behaviour. Alternatively the correlation between Z_N/Z_T increase and proppant injection suggests that the observed changes might be directly imaging proppant injection. Therefore our conclusions with respect to the cause of Z_N/Z_T variations are advanced tentatively. We anticipate that repeating such measurements on further hydraulic fracture stimulation data sets, in combination with a larger body of laboratory observations and modelling studies, will help improve our understanding of how Z_N/Z_T relates to fracturing and fluid/proppant injection processes. If we can do so, measurements of Z_N/Z_T made using SWS will help us to go 'beyond the dots in the box', providing more information to reservoir engineers during hydraulic fracture stimulation than the geometry of the fracture sets as revealed by event locations.

ACKNOWLEDGEMENTS

The authors would like to thank James Rutledge for providing the Cotton Valley microseismic data. Funding for the work has been provided by the sponsors of the Bristol University Microseismicity Projects (BUMPS). James Verdon is a Natural Environment Research Council (NERC) Early-Career Research Fellow (Grant Number NE/I021497/1).

REFERENCES

Angus D.A., Verdon J.P., Fisher Q.J. and Kendall J.-M. 2009. Exploring trends in microcrack properties of sedimentary rocks: An audit of dry core velocity-stress measurements. *Geophysics* **74**, E193–E203.

Backus G.E. 1962. Long-wave elastic anisotropy produced by horizontal layering. *Journal of Geophysical Research* **67**, 4427–4440.

Barton N. 2007. *Rock quality, seismic velocity, attenuation and anisotropy*. Taylor and Francis.

Batzle M.L., Simmons G. and Siegfried R.W. 1980. Microcrack closure in rocks under stress: Direct observation. *Journal of Geophysical Research* **85**, 7072–7090.

Chapman M. 2003. Frequency-dependent anisotropy due to mesoscale fractures in the presence of equant porosity. *Geophysical Prospecting* **51**, 369–379.

Crampin S., Volti T. and Stefánsson R. 1999. A successfully stress-forecast earthquake. *Geophysical Journal International* **138**, F1–F5.

Eisner L., Williams-Stroud S., Hill A., Duncan P. and Thornton M. 2010. Beyond the dots in the box: Microseismicity-constrained fracture models for reservoir simulation. *The Leading Edge* **29**, 326–333.

Hall S.A. and Kendall J.-M. 2000. Constraining the interpretation of AVOA for fracture characterisation. *in* Anisotropy 2000: Fractures, Converted Waves, and Case Studies. *Society of Exploration Geophysics* 107–144.

Hall S.A., Kendall J.-M., Maddock J. and Fisher Q. 2008. Crack density tensor inversion for analysis of changes in rock frame architecture. *Geophysical Journal International* **173**, 577–592.

Han D.-H., Nur A. and Morgan D. 1986. Effects of porosity and clay content on wave velocities in sandstones. *Geophysics* **51**, 2093–2107.

Herwanger J.V., Worthington M.H., Lubbe R., Binley A. and Khazanehdari J. 2004. A comparison of crosshole electrical and seismic data in fractured rock. *Geophysical Prospecting* **52**, 109–121.

Hobday C. and Worthington M.H. 2012. Field measurements of normal and shear fracture compliance. *Geophysical Prospecting* **60**, 488–499.

Hornby B.E. 1994. *The elastic properties of shales*. PhD thesis. Cambridge University.

Hsu C.-J. and Schoenberg M. 1993. Elastic waves through a simulated fractured medium. *Geophysics* **58**, 964–977.

Hudson J.A. 1981. Wave speeds and attenuation of elastic waves in material containing cracks. *Geophysical Journal of the Royal Astronomical Society* **64**, 133–150.

Hudson J.A., Liu E. and Crampin S. 1996a. The mechanical properties of materials with interconnected cracks and pores. *Geophysical Journal International* **124**, 105–112.

Hudson J.A., Liu E. and Crampin S. 1996b. Transmission properties of a fault plane. *Geophysical Journal International* **125**, 559–566.

Hudson J.A., Liu E. and Crampin S. 1997. The mean transmission properties of a fault with imperfect facial contact. *Geophysical Journal International* **129**, 720–726.

Hudson J.A., Pointer T. and Liu E. 2001. Effective medium theories for fluid saturated materials with aligned cracks. *Geophysical Prospecting* **49**, 509–522.

Jacoby H.D., O'Sullivan F.M. and Paltsev S. 2012. The influence of shale gas on U.S. energy and environmental policy. *Economics of Energy and Environmental Policy* **1**, 37–51.

Johnston J.E. and Christensen N.I. 1993. Compressional to shear velocity ratios in sedimentary rocks. *International Journal of Rock Mechanics and Mining Science* **30**, 751–754.

Laubach S.E. 1988. Subsurface fractures and their relationship to stress history in East Texas basin sandstone. *Tectonophysics* **156**, 37–49.

Laubach S.E. and Monson E.R. 1988. Coring-induced fractures: Indicators of hydraulic fracture propagation in a naturally fractured reservoir. (SPE 18164).

Lubbe R., Sothcott J., Worthington M.H. and McCann C. 2008. Laboratory estimates of normal and shear fracture compliance. *Geophysical Prospecting* **56**, 239–247.

MacBeth C. and Schuett H. 2007. The stress dependent elastic properties of thermally induced microfractures in aeolian Rotliegend Sandstone. *Geophysical Prospecting* **55**, 323–332.

Maxwell S.C. 2010. Microseismic: Growth born from success. *The Leading Edge* **29**, 338–343.

Nolen-Hoeksema R.C. and Ruff L.J. 2001. Moment tensor inversion of microseisms from the B-sand propped hydrofracture, M-site, Colorado. *Tectonophysics* **336**, 163–181.

Pointer T., Liu E. and Hudson J.A. 2000. Seismic wave propagation in cracked porous media. *Geophysical Journal International* **142**, 199–231.

Pyrak-Nolte L.J., Myer L.R. and Cook N.G.W. 1990. Transmission of seismic waves across single natural fractures. *Journal of Geophysical Research* **95**, 8617–8638.

Rathore J.S., Fjaer E., Holt R.M. and Renlie L. 1994. P- and S-wave anisotropy of a synthetic sandstone with controlled crack geometry. *Geophysical Prospecting* **43**, 711–728.

Rutledge J.T. and Phillips W.S. 2003. Hydraulic stimulation of natural fractures as revealed by induced microearthquakes, Carthage Cotton Valley gas field, East Texas. *Geophysics* **68**, 441–452.

Rutledge J.T., Phillips W.S. and Mayerhofer M.J. 2004. Faulting induced by forced fluid injection and fluid flow forced by faulting: An interpretation of hydraulic fracture microseismicity, Carthage Cotton Valley Gas Field, Texas. *Bulletin of the Seismological Society of America* **94**, 1817–1830.

Sambridge M. 1999a. Geophysical inversion with a neighbourhood algorithm I. Searching a parameter space. *Geophysical Journal International* **138**, 479–494.

Sambridge M. 1999b. Geophysical inversion with a neighbourhood algorithm II. Appraising the ensemble. *Geophysical Journal International* **138**, 727–746.

Sayers C.M. 1999. Stress-dependent seismic anisotropy of shales. *Geophysics* **64**, 93–98.

Sayers C.M. and den Boer L.D. 2012. Characterizing production-induced anisotropy of fractured reservoirs having multiple fracture sets. *Geophysical Prospecting* ??, ??–??

Sayers C.M. and Han D.-H. 2002. The effect of pore fluid on the stress-dependent elastic wave velocities in sandstones. *SEG Expanded Abstracts* **21**, 1842–1845.

Sayers C.M. and Kachanov M. 1995. Microcrack induced elastic wave anisotropy of brittle rocks. *Journal of Geophysical Research* **100**, 4149–4156.

Sayers C.M., Taleghani A.D. and Adachi J. 2009. The effect of mineralization on the ratio of normal to tangential compliance of fractures. *Geophysical Prospecting* **57**, 439–446.

Schoenberg M. and Sayers C.M. 1995. Seismic anisotropy of fractured rock. *Geophysics* **60**, 204–211.

Teanby N.A., Kendall J.-M. and van der Baan M. 2004. Automation of shear-wave splitting measurements using cluster analysis. *Bulletin of the Seismological Society of America* **94**, 453–463.

Thomsen L. 1986. Weak elastic anisotropy. *Geophysics* **51**, 1954–1966.

Urbancic T.I. and Rutledge J. 2000. Using microseismicity to map Cotton Valley hydraulic fractures. *SEG Expanded Abstracts* **19**, 1444–1448.

Valcke S.L.A., Casey M., Lloyd G.E., Kendall J.-M. and Fisher Q. J. 2006. Lattice preferred orientation and seismic anisotropy in sedimentary rocks. *Geophysical Journal International* **166**, 652–666.

Verdon J.P., Angus D.A., Kendall J.-M. and Hall S.A. 2008. The effects of microstructure and nonlinear stress on anisotropic seismic velocities. *Geophysics* **73**, D41–D51.

Verdon J.P. and Kendall J.-M. 2011. Detection of multiple fracture sets using observations of shear-wave splitting in microseismic data. *Geophysical Prospecting* **59**, 593–608.

Verdon J.P., Kendall J.-M. and Wüstefeld A. 2009. Imaging fractures and sedimentary fabrics using shear wave splitting measurements made on passive seismic data. *Geophysical Journal International* **179**, 1245–1254.

Vernik L. 1993. Microcrack-induced versus intrinsic elastic anisotropy in mature HC-source rocks. *Geophysics* **58**, 1703–1706.

Vlastos S., Liu E., Main I.G., Schoenberg M., Narteau C., Li X.-Y. and Maillot B. 2006. Dual simulations of fluid flow and seismic wave propagation in a fractured network: Effects of pore pressure on seismic signature. *Geophysical Journal International* **166**, 825–838.

Walker R.N. 1997. Cotton Valley hydraulic fracture imaging project. (SPE 38577).

Wessels S.A., De La Peña A., Kratz M., Williams-Stroud S. and Jbeili T. 2011. Identifying faults and fractures in unconventional reservoirs through microseismic monitoring. *First Break* **29**, 99–104.

Wookey J. 2012. Direct probabilistic inversion of shear-wave data for anisotropy. *Geophysical Journal International* **189**, 1025–1037.

Worthington M. 2007. The compliance of macrofractures. *The Leading Edge* **26**, 1118–1122.

Worthington M.H. and Lubbe R. 2007. The scaling of fracture compliance, in Fractured Reservoirs. *Geological Society of London Special Publication* 73–82.

Wüstefeld A., Al Harrasi O., Verdon J.P., Wookey J. and Kendall J.-M. 2010. A strategy for automated analysis of passive microseismic data to image seismic anisotropy and fracture characteristics. *Geophysical Prospecting* **58**, 755–773.

Wüstefeld A., Kendall J.-M., Verdon J.P. and van As A. 2011a. In-situ monitoring of rock fracturing using shear-wave splitting analysis: An example for a mining setting. *Geophysical Journal International* **187**, 848–860.

Wüstefeld A., Verdon J., Kendall J.-M., Rutledge J., Clarke H. and Wookey J. 2011b. Inferring rock fracture evolution during reservoir stimulation from seismic anisotropy. *Geophysics* **76**, WC157–WC166.

Yoshioka N. and Scholz C.H. 1989a. Elastic properties of contacting surfaces under normal and shear loads: 1. Theory. *Journal of Geophysical Research* **94**, 17681–17690.

Yoshioka N. and Scholz C.H. 1989b. Elastic properties of contacting surfaces under normal and shear loads: 2. Comparison of theory with experiment. *Journal of Geophysical Research* **94**, 17691–17700.